Exp Fluids (2007) 42:385–401
DOI 10.1007/s00348-006-0246-2

RESEARCH ARTICLE

Turbulent time and length scale measurements in high-velocity open channel flows

Hubert Chanson · Giovanna Carosi

Received: 18 September 2006 / Revised: 7 December 2006 / Accepted: 8 December 2006 / Published online: 26 January 2007

Abstract In high-velocity open channel flows, the measurements of air–water flow properties are complicated by the strong interactions between the flow turbulence and the entrained air. In the present study, an advanced signal processing of traditional single- and dual-tip conductivity probe signals is developed to provide further details on the air–water turbulent level, time and length scales. The technique is applied to turbulent open channel flows on a stepped chute conducted in a large-size facility with flow Reynolds numbers ranging from 3.8E+5 to 7.1E+5. The air water flow properties presented some basic characteristics that were qualitatively and quantitatively similar to previous skimming flow studies. Some self-similar relationships were observed systematically at both macroscopic and microscopic levels. These included the distributions of void fraction, bubble count rate, interfacial velocity and turbulence level at a macroscopic scale, and the auto- and cross-correlation functions at the microscopic level. New correlation analyses yielded a characterisation of the large eddies advecting the bubbles. Basic results included the integral turbulent length and time scales. The turbulent length scales characterised some measure of the size of large vortical structures advecting air bubbles in the skimming flows, and the data were closely related to the characteristic air–water depth Y_{90}. In the spray region, present results highlighted the existence of an upper spray region for $C > 0.95$–0.97 in which the distributions of droplet chord sizes and integral advection scales presented some marked differences with the rest of the flow.

H. Chanson (✉) · G. Carosi
Division of Civil Engineering,
The University of Queensland,
Brisbane, QLD 4072, Australia
e-mail: h.chanson@uq.edu.au

List of symbols

C	void fraction defined as the volume of air per unit volume of air and water; it is also called air concentration or local air content
C_{mean}	depth-average void fraction defined in terms of Y_{90}: $C_{mean} = 1 - d/Y_{90}$
D_H	hydraulic diameter (m) also called equivalent pipe diameter
D_o	dimensionless constant
d	equivalent clear water flow depth defined as $d = \int_{C=0}^{C=0.90} (1 - C)\,dy$
d_c	critical flow depth (m): $d_c = \sqrt[3]{Q_w^2/(gW^2)}$
F	air bubble count rate (Hz) or bubble frequency defined as the number of detected air bubbles per unit time
F_{max}	maximum bubble count rate (Hz) at a cross-section
g	gravity constant: $g = 9.80$ m/s^2 in Brisbane, Australia
h	vertical step height (m)
K'	dimensionless integration constant
K^*	dimensionless constant
L_{xx}	air–water advection integral length scale (m): $L_{xx} = VT_{xx}$
L_{xy}	transverse/streamwise air–water integral turbulent length scale (m): $L_{xy} = \int_{Y=0}^{Y_{max}} (R_{xy})_{max}\,dY$
$(L_{xx})_{max}$	maximum advection air–water length scale (m) in a cross-section

$(L_{xy})_{max}$ maximum air–water integral length scale (m) in a cross-section
l horizontal step length (m)
N power law exponent
Q_w water discharge (m^3/s)
Re Reynolds number defined in terms of the hydraulic diameter
R_{xx} normalised auto-correlation function
R_{xy} normalised cross-correlation function between two probe output signals
$(R_{xy})_{max}$ maximum cross-correlation between two probe output signals
S_o bed slope: $S_o = \sin\theta$
T time lag (s) for which $R_{xy} = (R_{xy})_{max}$
$\mathbf{T}$ integral turbulent time scale (s) characterising large eddies advecting the air bubbles
Tu turbulence intensity defined as $Tu = u'/V$
T_{xx} auto-correlation time scale (s): $T_{xx} = \int_{\tau=0}^{\tau=\tau(R_{xx}=0)} R_{xx}(\tau)\,d\tau$
T_{xy} cross-correlation time scale (s): $T_{xy} = \int_{\tau=\tau(R_{xy}=(R_{xy})_{max})}^{\tau=\tau(R_{xy}=0)} R_{xy}(\tau)\,d\tau$
$T_{0.5}$ characteristic time lag (s) for which $R_{xx} = 0.5$
$\mathbf{T}_{max}$ maximum integral time scale (s) in a cross-section
(T_{xy}) maximum cross-correlation time scale (s) in a cross-section
U_w flow velocity (m/s): $U_w = Q_w/(dW)$
u' root mean square of longitudinal component of turbulent velocity (m/s)
V interfacial velocity (m/s)
V_c critical flow velocity (m/s)
V_{90} characteristic interfacial velocity (m/s) where $C = 0.90$
W channel width (m)
x distance along the channel bottom (m)
Y separation distance (m) between two phase-detection probe sensors
Y_{90} characteristic depth (m) where the void fraction is 90%
y distance (m) measured normal to the invert (or channel bed)
y' dimensionless distance (m) normal to the invert (or channel bed): $y' = y/Y_{90}$
z transverse distance (m) from the channel centreline

Greek symbols

Δx streamwise separation distance (m) between sensor
Δz transverse separation distance (m) between sensor
μ dynamic viscosity (Pa s)
μ_w water dynamic viscosity (Pa s)
θ angle between the pseudo-bottom formed by the step edges and the horizontal
ρ density (kg/m^3)
ρ_w water density (kg/m^3)
τ time lag (s)
$\tau_{0.5}$ characteristic time lag τ for which $R_{xy} = 0.5(R_{xy})_{max}$
χ dimensionless parameter: $\chi = K' - y'/(2D_o) + (y' - 1/3)^3/(3D_o)$
Ø diameter (m)

Subscript

w water flow
xx auto-correlation of reference probe signal
xy cross-correlation
90 flow conditions where $C = 0.90$

1 Introduction

In high-velocity open channel flows, the strong interactions between the turbulent waters and the atmosphere lead often to some air bubble entrainment. The entrained air is advected within the bulk of the flow and the air–water mixture has a whitish appearance (Fig. 1a). In civil engineering applications, the flow velocity exceeds typically 5–10 m/s, and the flow Reynolds number ranges from 1E+7 to over 1E+9 in large dam spillways. The void fraction ranges from 100% above the ''free-surface'' to some small, often non-zero value close to the invert (e.g. Cain and Wood 1981b). These high-velocity, highly-aerated flows cannot be studied analytically nor numerically because of the large number of relevant equations and parameters. Present knowledge relies upon physical modelling and experimental measurements. Accurate measurement systems for air–water flow measurements include intrusive phase-detection probes, hot-film probes, and LDA/PDA systems. Authoritative reviews include Jones and Delhaye (1976), Cain and Wood (1981a), Chanson (1997a, 2002) and Chang et al. (2003). The processing of these measurement techniques yield basically the void fraction, bubble count rate, interfacial velocity and turbulence intensity. Further information requires more advanced instrumentation: e.g., 4- or 5-sensor probes (Kim et al. 2000; Euh et al. 2006).

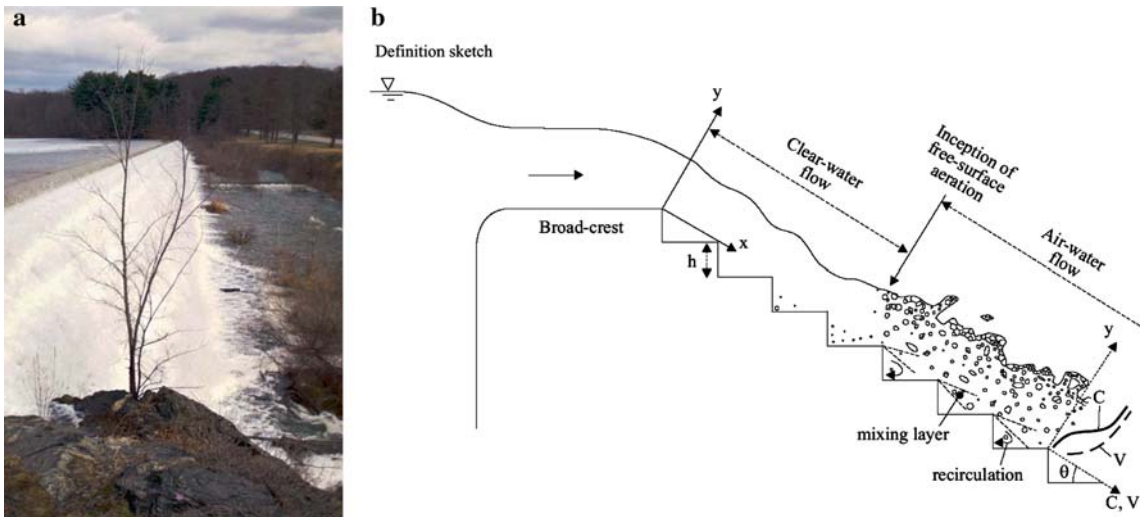

Fig. 1 Skimming flows on a stepped chute. **a** Skimming flow on Croton Falls dam stepped spillway (h = 0.6 m) in March 2001 (Courtesy of Mrs Jenny Hacker). **b** Definition sketch

In the present study, it is shown that an advanced signal processing of traditional single- and dual-tip conductivity probes may provide further information on the air–water turbulent time and length scales. The technique was applied to turbulent open channel flows on a stepped chute. The measurements were conducted in a large-size facility (θ = 22°, h = 0.1 m) in which detailed air–water flow properties were recorded systematically for several flow rates including turbulence levels and turbulent time and length scales.

2 Experimental apparatus and procedures

2.1 Experimental flume

New experiments were performed a 3.2 m long 1 m wide flume with an average bed slope $S_o \approx 0.37$ (θ = 21.8°) and a stepped invert (Fig. 1b). Previous experiments were conducted in the same channel by Chanson and Toombes (2001, 2002) and Gonzalez (2005). Waters were supplied from a large feeding basin leading to a sidewall convergent with a 4.8:1 contraction ratio. The test section consisted of a broad-crested weir (1 m wide, 0.6 m long, with upstream rounded corner) followed by ten identical steps (h = 0.1 m, l = 0.25 m) made of marine ply. The stepped chute was 1 m wide with perspex sidewalls followed by a horizontal concrete canal ending in a sump pit.

The water was delivered by a pump controlled with an adjustable frequency AC motor drive, enabling an accurate discharge adjustment in a closed-circuit system. Further details and the full data set were reported by Carosi and Chanson (2006).

2.2 Instrumentation

Clear-water flow depths were measured with a point gauge. The discharge was measured from the upstream head above the crest with an accuracy of about 2%. The discharge measurements were derived from Gonzalez (2005) detailed velocity distribution measurements on the broad-crested weir.

The air–water flow properties were measured with two types of conductivity probes: single-tip and dual-tip probes (Fig. 2). Basic air–water flow measurements were performed with the single-tip conductivity probes (needle probe design). Figure 2a shows two single-tip conductivity probes side-by-side. Each probe consisted of a sharpened rod (Ø = 0.35 mm) coated with non-conductive epoxy set into a stainless steel surgical needle acting as the second electrode. Additional measurements were performed with some double-tip conductivity probes (Fig. 2b). Each sensor consisted of a sharpened rod (platinum wire Ø = 0.25 mm). The longitudinal spacing between the probe sensors was measured with a microscope and this yielded Δx = 7.0 and 9.6 mm for each of the double-tip probes.

All the probes were excited by an electronic system (Ref. UQ82.518) designed with a response time less than 10 μs and calibrated with a square wave generator. The measurements were conducted on the channel centreline (z = 0). For some experiments, a second identical probe was placed beside the first one with the probe sensors at the same vertical and streamwise distances y and x, respectively, and separated by a transverse distance Δz (Fig. 2).

For all experiments, each probe sensor was scanned at 20 kHz for 45 s.

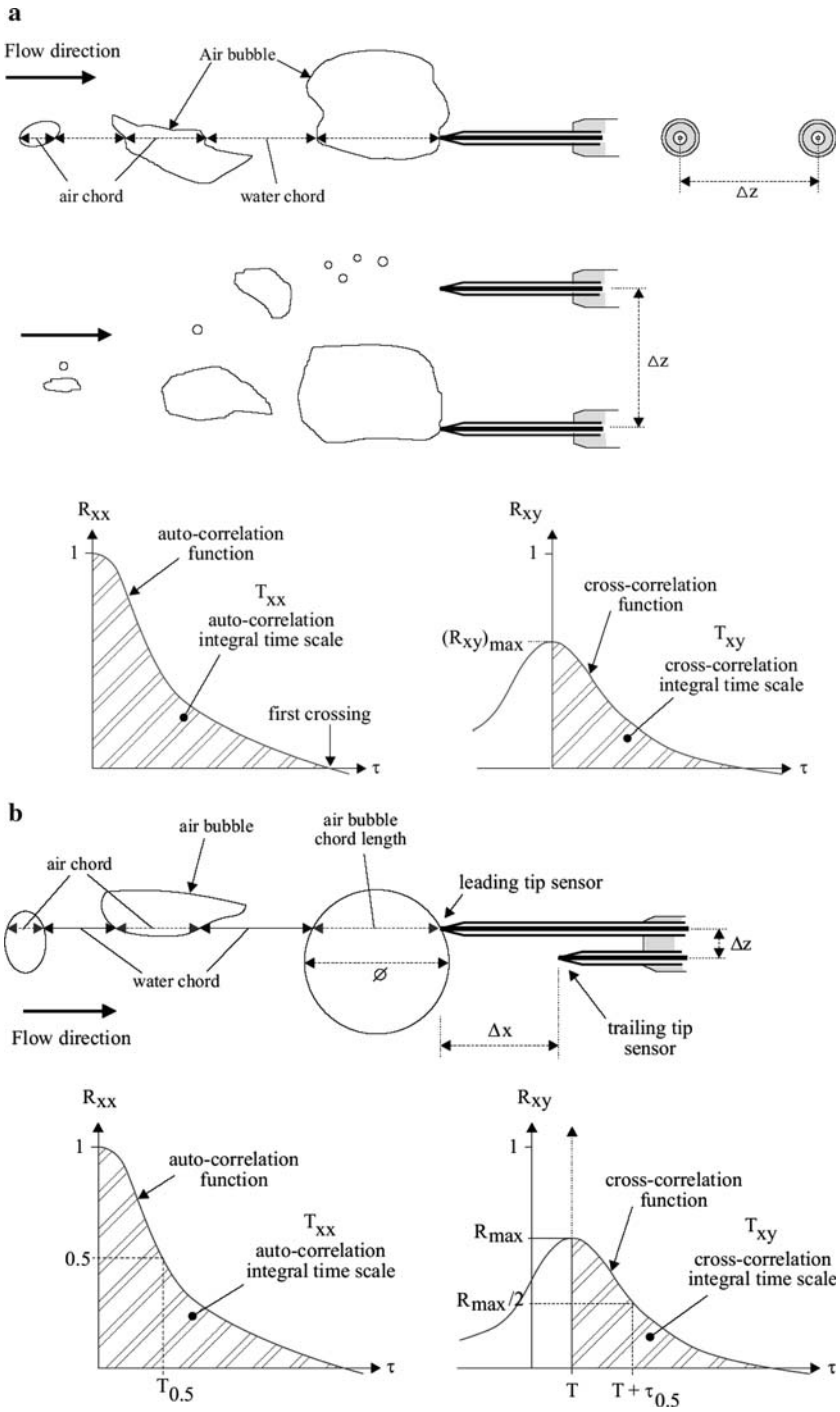

Fig. 2 Definition sketch of the phase-detection conductivity probes. **a** Two single-tip conductivity probes side-by-side. **b** Dual-tip conductivity probe

2.3 Signal processing

The measurement principle of conductivity probes is based upon the difference in electrical resistivity between air and water. Since the resistance of water is one thousand times lower than the resistance of air, the time-variation of the voltage output has a ''square-wave'' shape. Each steep drop of the signal corresponds to an air bubble pierced by the probe tip. Herein the air–water flow properties were calculated using a single threshold technique for all void fractions. The threshold was set at about 45–55% of the air–water voltage range. A sensitivity analysis was conducted with thresholds between 40 and 60% of the voltage range, and the results showed little effect of threshold on the air–water flow properties (Toombes 2002). A similar finding was

obtained by Herringe and Davis (1974) with threshold between 20 and 70% of the air–water voltage range.

The air concentration or void fraction C is the proportion of time that the probe tip is in the air. The bubble count rate F is the number of bubbles impacting the probe tip per second. The air–water interfacial velocities were deduced from a correlation analysis between the two sensors of the dual-tip probe (Chanson 1997a, 2002; Crowe et al. 1998). The time averaged interfacial velocity equals:

$$V = \frac{\Delta x}{T} \quad (1)$$

where T is the air–water interfacial travel time for which the cross-correlation function is maximum and Δx the longitudinal distance between probe sensors (Fig. 2b). Turbulence levels may be derived from the relative width of the cross-correlation function:

$$\mathrm{Tu} = 0.851 \frac{\sqrt{\tau_{0.5}^2 - T_{0.5}^2}}{T} \quad (2)$$

where $\tau_{0.5}$ is the time scale for which the cross-correlation function is half of its maximum value, such as $R_{xy}(T + \tau_{0.5}) = 0.5 R_{xy}(T)$, R_{xy} is the normalised cross-correlation function, and $T_{0.5}$ is the characteristic time for which the normalised auto-correlation function equals: $R_{xx}(T_{0.5}) = 0.5$ (Fig. 2b). While Eq. 2 might not be equal to the turbulence intensity u'/V, it is an expression of some turbulence level and average velocity fluctuations (Chanson and Toombes 2002).

More generally, when two probe sensors are separated by a transverse or streamwise distance Y, their signals may be analysed in terms of the auto-correlation and cross-correlation functions R_{xx} and R_{xy}, respectively (Fig. 2). Herein the original data of 900,000 samples were segmented into fifteen non-overlapping segments of 60,000 samples because the periodogram resolution is inversely proportional to the number of samples and it could be biased with large data sets (Hayes 1996; Gonzalez 2005). Further, the correlation analyses were conducted on the raw probe output signals. Basic correlation analysis results included the maximum cross-correlation coefficient $(R_{xy})_{max}$, and the correlation times T_{xx} and T_{xy}, where

$$T_{xx} = \int_{\tau=0}^{\tau=\tau(R_{xx}=0)} R_{xx}(\tau)\,\mathrm{d}\tau \quad (3)$$

$$T_{xy} = \int_{\tau=\tau(R_{xy}=(R_{xy})_{max})}^{\tau=\tau(R_{xy}=0)} R_{xy}(\tau)\,\mathrm{d}\tau \quad (4)$$

where R_{xx} is the normalised auto-correlation function, t the time lag, and R_{xy} the normalised cross-correlation function between the two probe output signals (Fig. 2). The auto-correlation integral time T_{xx} characterises the longitudinal bubbly flow structure. The cross-correlation time scale T_{xy} is a function of the probe separation distance Y. The probe separation distance Y is also denoted Δz for the transverse separation distance and Δx for the streamwise separation.

In the present study, identical experiments were repeated with several separation distances Y ($Y = \Delta z$ or Δx) (Table 1). An integral length scale may be derived as

$$L_{xy} = \int_{Y=0}^{Y=Y((R_{xy})_{max}=0)} (R_{xy})_{max}\,\mathrm{d}Y \quad (5)$$

The corresponding integral time scale is:

Table 1 Summary of experimental flow conditions on the stepped chute

References	θ (deg)	h (m)	Q_w (m^3/s)	$\frac{d_c}{h}$	Re	Instrumentation	Comments
Chanson and Toombes (2001, 2002)	15.9	0.1	0.07–0.18	0.78–1.53	2.7–7.5E+5	Dual-tip probe (Ø = 0.025 mm)	Δx = 8 mm
	21.8	0.1	0.06–0.18	0.7–1.5	2.3–7.3E+3		
Gonzalez (2005)	15.9	0.05	0.02–0.2	0.7–3.2	0.79–8E+5	Dual-tip probe (Ø = 0.025 mm)	Δx = 8 mm
	15.9	0.1	0.08–0.2	0.6–1.7	3.2–8E+5		
	21.8	0.1	0.09–0.18	1.0–1.5	3.8–7.1E+5		
Present study	21.8	0.1	0.09–0.18	1.0–1.57	3.8–7.1E+5	Single-tip probes (Ø = 0.35 mm)	W = 1 m Δz = 3.6–55.7 mm
						Dual-tip probe (Ø = 0.25 mm)	Δx = 7.0 and 9.6 mm Δz = 1.4 mm

d_c Critical flow depth, h step height, Re Reynolds number defined in terms of the hydraulic diameter

$$\mathbf{T} = \frac{\int_{Y=0} (R_{xy})_{max} T_{xy}\, dy}{L_{xy}} \quad (6)$$

An advection integral length scale is

$$L_{xx} = V T_{xx} \quad (7)$$

where V is the advective velocity magnitude. The physical significance of L_{xy}, $\mathbf{T}$ and L_{xx} is discussed later.

2.4 Initial flow conditions

Experiments were conducted for a range of flow rates although the focus was on the highly aerated skimming flows (Table 1). Detailed measurements were performed for flow rates between 0.09 and 0.18 m^3/s corresponding to dimensionless discharges d_c/h = 1.0–1.57 and flow Reynolds numbers $Re = \rho_w U_w D_H / \mu_w$ between 3.8E+5 and 7.1E+5, where d_c is the critical flow depth, h the step height, U_w the depth-averaged velocity, D_H the hydraulic diameter, and ρ_w and μ_w are the water density and dynamic viscosity, respectively. Present measurements were performed systematically at step edges downstream of the inception point of free-surface aeration (Fig. 1b).

3 Experimental results

3.1 Basic flow patterns

The basic flow regimes were inspected in a series of preliminary experiments with discharges ranging from 0.008 to 0.180 m^3/s. For small flow rates (Re < 1.4E+5), the waters flowed as a succession of free-falling jets that was typical of a nappe flow regime. For some intermediate discharges (1.4E+5 < Re < 3.6E+5), the flow had a chaotic behaviour characterised by strong splashing and droplet projections downstream of the inception point of free-surface aeration. For larger flows (Re > 3.6E+5), the waters skimmed above the pseudo-bottom formed by the step edges (Fig. 1). The skimming flows were characterised by strong cavity recirculation with three-dimensional vortical patterns. These were best seen next to the inception point of free-surface aeration. Overall the results in terms of flow regimes and changes between flow regimes were very close to the earlier observations of Chanson and Toombes (2001) and Gonzalez (2005) in the same facility.

3.2 Distributions of void fraction and bubble count rate

Experimental observations demonstrated substantial free-surface aeration immediately downstream of the inception point of free-surface aeration while some sustained flow aeration was observed further downstream. This is illustrated in Fig. 3 where the dimensionless distributions for void fraction C and bubble count rate Fd_c/V_c are presented as functions of y/Y_{90} for several successive step edges for the same flow rate, where y is the distance normal to the pseudo-bottom formed by the step edges, Y_{90} is the characteristic distance where C = 0.90, and d_c and V_c are, respectively, the critical flow depth and velocity defined as

$$d_c = \sqrt[3]{\frac{Q_w^2}{gW^2}} \quad (8)$$

$$V_c = \sqrt{g d_c} \quad (9)$$

with Q_w the water discharge, g the gravity acceleration and W the channel width. For the data shown in Fig. 3a, the flow aeration was nil at step edge 6 immediately upstream of the inception point. Between step edges 6 and 7, some strong self-aeration took place. The amount of entrained air and the mean air content were about constant between the step edges 7 and 10, and the depth-averaged void fraction C_{mean} was about 0.35–0.37.

The void fraction profiles showed consistently a similar shape (Fig. 3). The dimensionless distributions exhibited a S-shape profile that was observed in previous skimming flow studies: e.g., Ruff and Frizell (1994), and Chanson and Toombes (1997). For all the data, the void fraction distribution measurements compared well with an analytical solution of the advective diffusion equation for air bubbles:

$$C = 1 - \tanh^2\left(K' - \frac{\frac{y}{Y_{90}}}{2D_o} + \frac{\left(\frac{y}{Y_{90}} - \frac{1}{3}\right)^3}{3D_o}\right) \quad (10)$$

where K' is an integration constant and D_o is a function of the depth-averaged void fraction C_{mean} only:

$$K' = K^* + \frac{1}{2D_o} - \frac{8}{81 D_o} \quad (11)$$

$$K^* = \tanh^{-1}(\sqrt{0.1}) = 0.32745015\ldots \quad (12)$$

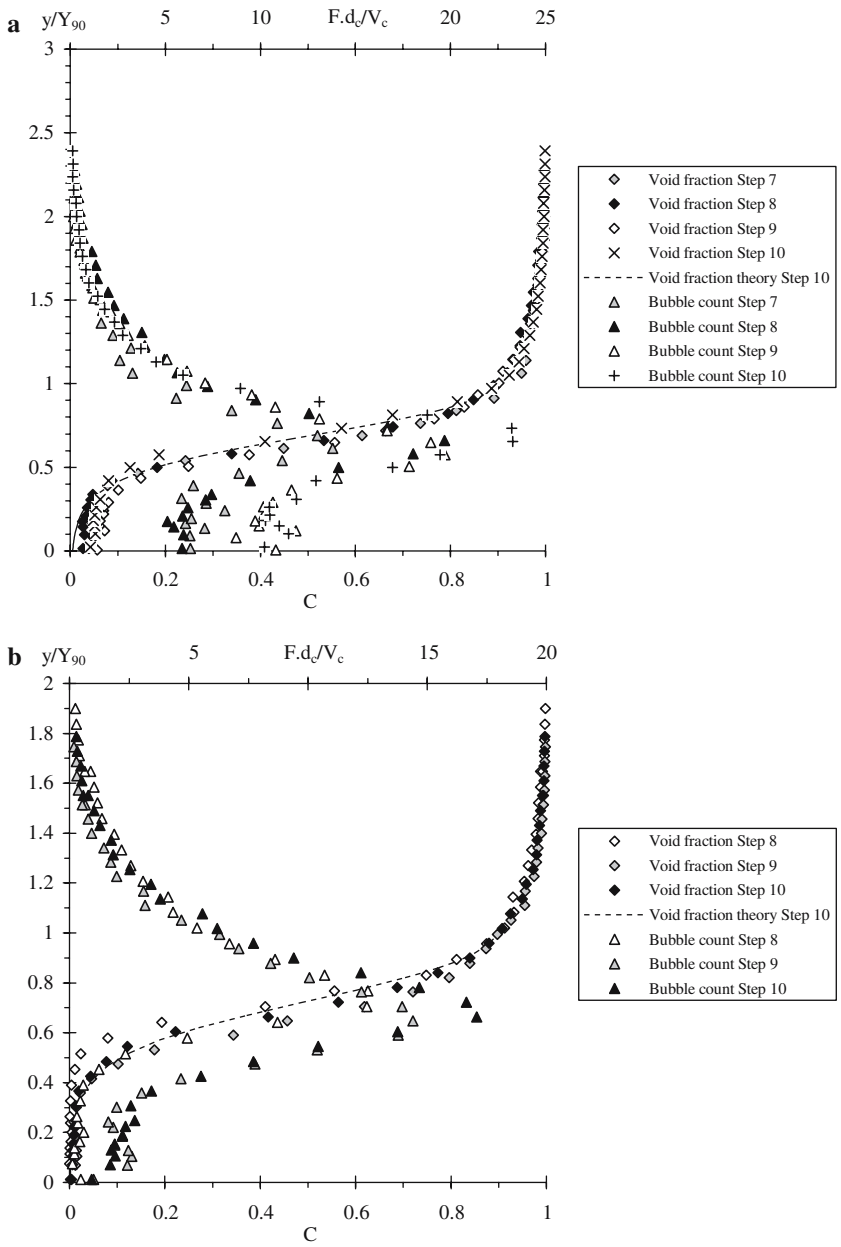

Fig. 3 Dimensionless distributions of void fraction C and bubble count rate Fd_c/V_c as functions of y/Y_{90}—comparison between Eq. 10 and void fraction data. **a** $d_c/h = 1.33$, double-tip probe (Ø = 0.25 mm). **b** $d_c/h = 1.57$, single-tip probe (Ø = 0.35 mm)

$$C_{mean} = \frac{1}{Y_{90}} \int_{y=0}^{Y_{90}} C\,dy = 0.7622(1.0434 - \exp(-3.614D_0)) \quad (13)$$

Equation 10 was first developed by Chanson and Toombes (2002) and is compared with dimensionless void fraction data in Fig. 3.

The dimensionless distributions of bubble count rate showed consistently a characteristic shape with a maximum value observed for void fractions between 40 and 60% (Fig. 3). A similar result was observed in smooth chute and stepped spillway flows (e.g. Chanson 1997b; Chanson and Toombes 2002; Toombes 2002). The relationship between bubble frequency and void fraction was approximated by a parabolic shape:

$$\frac{F}{F_{max}} = 4C(1 - C) \quad (14)$$

For the present study, the maximum bubble count rate F_{max} was observed for $0.35 \leq C \leq 0.6$ although most data sets were within $0.4 \leq C \leq 0.5$. Toombes (2002) demonstrated some theoretical validity of Eq. 14 and he extended the reasoning to air–water flow situations when the maximum bubble count rate is observed for $C \neq 0.5$ (Toombes 2002, pp 190–195).

3.3 Distributions of interfacial velocity and turbulence level

At each step edge, the time-averaged velocity and turbulent velocity fluctuation profiles showed some characteristic shapes (Fig. 4a). The interfacial velocity distributions presented a smooth shape similar to earlier results on stepped chutes (e.g. Boes 2000; Chanson and Toombes 2002; Gonzalez 2005). Importantly, the velocity distributions showed some self-similarity (Fig. 4b). All the data followed closely a power-law function for $y/Y_{90} \leq 1$. For $y/Y_{90} > 1$, the velocity profile was quasi-uniform. That is

$$\frac{V}{V_{90}} = \left(\frac{y}{Y_{90}}\right)^{1/N} \quad 0 \leq \frac{y}{Y_{90}} \leq 1 \tag{15}$$

$$\frac{V}{V_{90}} = 1 \quad 1 \leq \frac{y}{Y_{90}} \leq 2.5 \tag{16}$$

where V_{90} is the characteristic air–water velocity at $y = Y_{90}$. Several researchers observed the velocity profile described by Eq. 15, but few studies documented the velocity distribution in the upper spray region (Gonzalez 2005). Present data are compared with Eqs. 15 and 16 in Fig. 4b. For the present experiments, the exponent N was about 10, although it varied between a step edge and the next consecutive step edge for a given flow rate. The variations was believed to reflect some flow interactions between adjacent shear layers and cavity flows.

In the upper flow region (i.e. $y > Y_{90}$), the data showed a quasi-uniform velocity profile (Eq. 16). The finding was consistent with visual observations of the flow structure consisting predominantly of individual water droplets and packets surrounded by air. The result tended to suggest that most spray droplets were in a free-fall trajectory since the ejected droplets had a response time of nearly two orders of magnitude larger than that of the surrounding air flow.

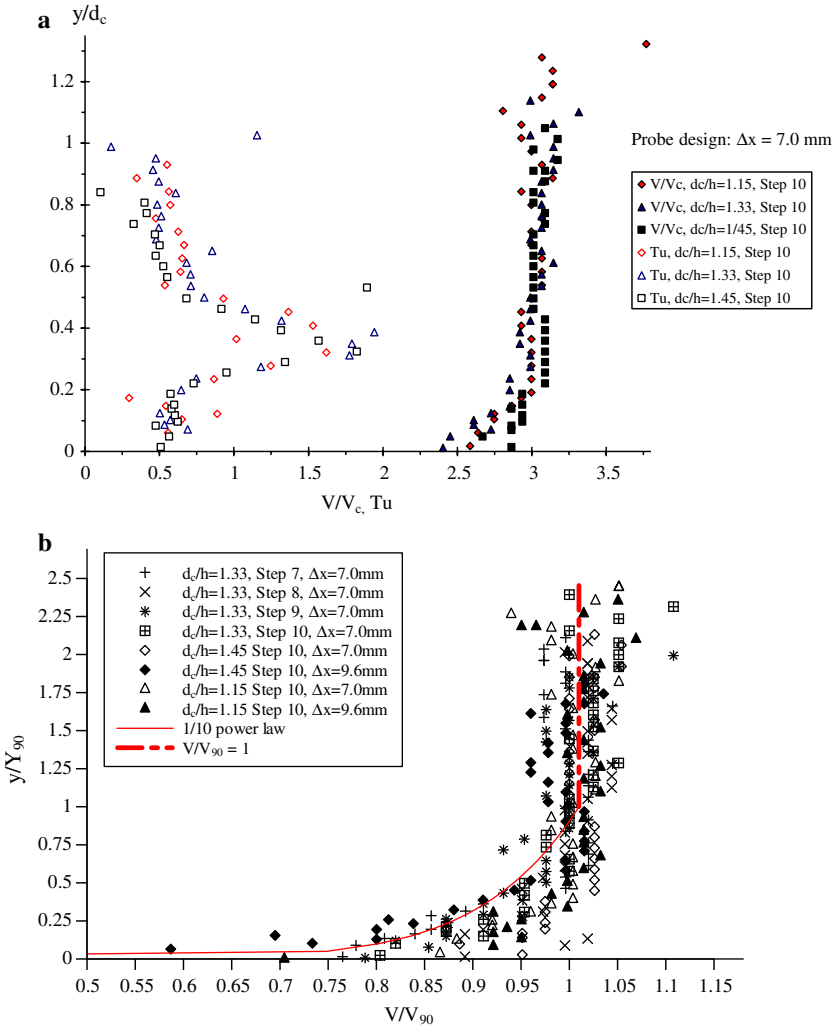

Fig. 4 Dimensionless distributions of turbulent velocity. **a** Distributions of time-averaged interfacial velocity V/V_c and turbulence intensity Tu for $d_c/h =$ 1.15, 1.33 and 1.45 at step edge 10. **b** Distributions of time-averaged interfacial velocity distributions V/V_{90}—comparison with a 1/10 power law (Eq. 15) and with Eq. 16

The turbulent intensity profiles exhibited some maximum turbulence level for $0.3 \leq y/d_c \leq 0.4$ which corresponded to about $C \approx 0.4$–0.6 (Fig. 4a). The experimental data showed further a strong correlation between the turbulence intensity Tu and the bubble count rate. This is illustrated in Fig. 5 presenting the turbulence intensity Tu as a function of the dimensionless bubble count rate Fd_c/V_c. The data collapsed reasonably well into a single curve:

$$\mathrm{Tu} = 0.25 + 0.035\left(\frac{Fd_c}{V_c}\right)^{1.2} \quad (17)$$

Equation 17 reflects a monotonic increase in turbulence levels with an increase in bubble count rate. The limit for $F = 0$ (i.e. Tu = 0.25) is close to monophase flow measurements on a stepped chute upstream of the inception point of free-surface aeration (Ohtsu and Yasuda 1997; Amador et al. 2004). It is hypothesised that the large number of air–water interfaces, and the continuous deformations of the air–water interfacial structure generated large turbulence levels measured by the intrusive phase-detection probe (i.e. double-tip conductivity probe).

3.4 Correlation functions and time scales

The correlation functions exhibited similar patterns for all investigated flow conditions with both transverse and longitudinal separations. The auto-correlation functions were best fitted by

$$R_{xx} = \frac{1}{1 + \left(\frac{\tau}{T_{0.5}}\right)^{1.3}} \quad (18)$$

where τ is the time lag and $T_{0.5}$ is the time lag for which $R_{xx} = 0.5$. The cross-correlation functions exhibited clearly a marked maximum $(R_{xy})_{max}$ which decreased with increasing sensor separation Y as illustrated in Fig. 6. $(R_{xy})_{max}$ reached the largest values for $C = 0.4$–0.6, and this is linked to the presence of maximum bubble count rate. The cross-correlation functions followed closely a Gaussian error function:

$$\frac{R_{xy}}{(R_{xy})_{max}} = \exp\left(-\frac{1}{1443}\frac{(\tau - T)^2}{\tau_{0.5}}\right) \quad \frac{\tau - T}{\tau_{0.5}} < 2 \quad (19)$$

where $(R_{xy})_{max}$ is the maximum normalised cross-correlation value observed for the time lag $\tau = T$, and $\tau_{0.5}$ is the time lag for which $R_{xy} = 0.5(R_{xy})_{max}$ (Fig. 2). The finding (Eq. 19) was observed systematically for $(\tau - T)/\tau_{0.5} < 2$. Note that some earlier studies reported streamwise cross-correlation function data that followed similarly a Gaussian error function (e.g. Chanson 2002; Chanson and Toombes 2002).

Typical distributions of correlation time scales T_{xx} and T_{xy} are presented in Fig. 7. Figure 7a shows the vertical distributions of correlation time scales for several transverse spacings with identical flow conditions. Note that the correlation time scales are presented in a dimensional form (units: s). T_{xx} represents a time scale of the longitudinal bubbly flow structure and of the eddies advecting the air–water interfaces in the streamwise direction. The cross-correlation time scale T_{xy} represents a characteristic time of the vortices with a length scale Y advecting the air–water structures where the length scale Y is the probe separation distance.

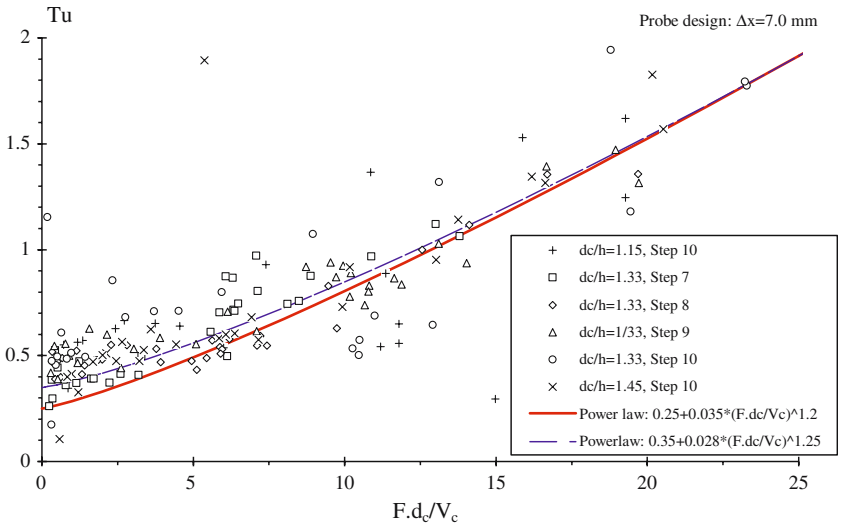

Fig. 5 Dimensionless relationship between turbulence intensity Tu and bubble count rate Fd_c/V_c—comparison between data and Eq. 17

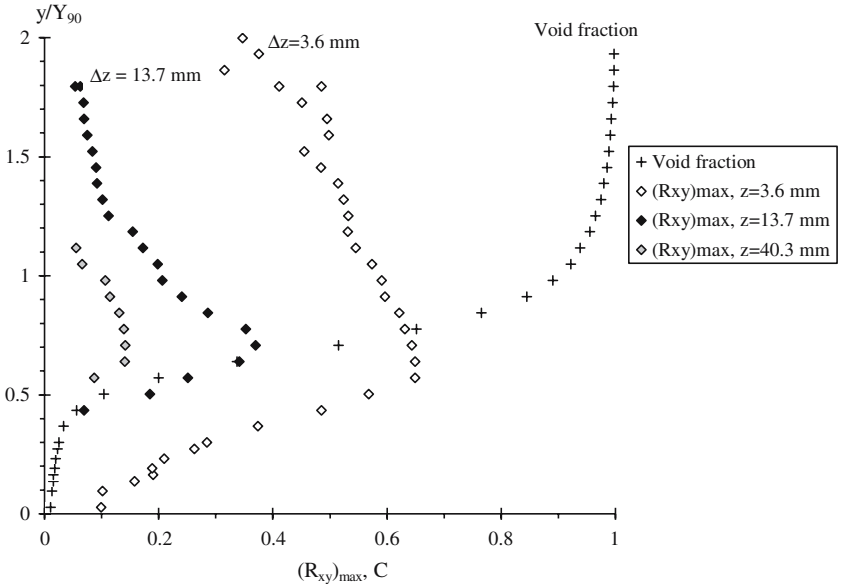

Fig. 6 Dimensionless distributions of maximum cross-correlation coefficients $(R_{xy})_{max}$ between two probe sensors separated by a transverse distance Δz—flow conditions: d_c/h = 1.45, Re = 6.4E+5, single-tip probe (Ø = 0.35 mm), step edge 10

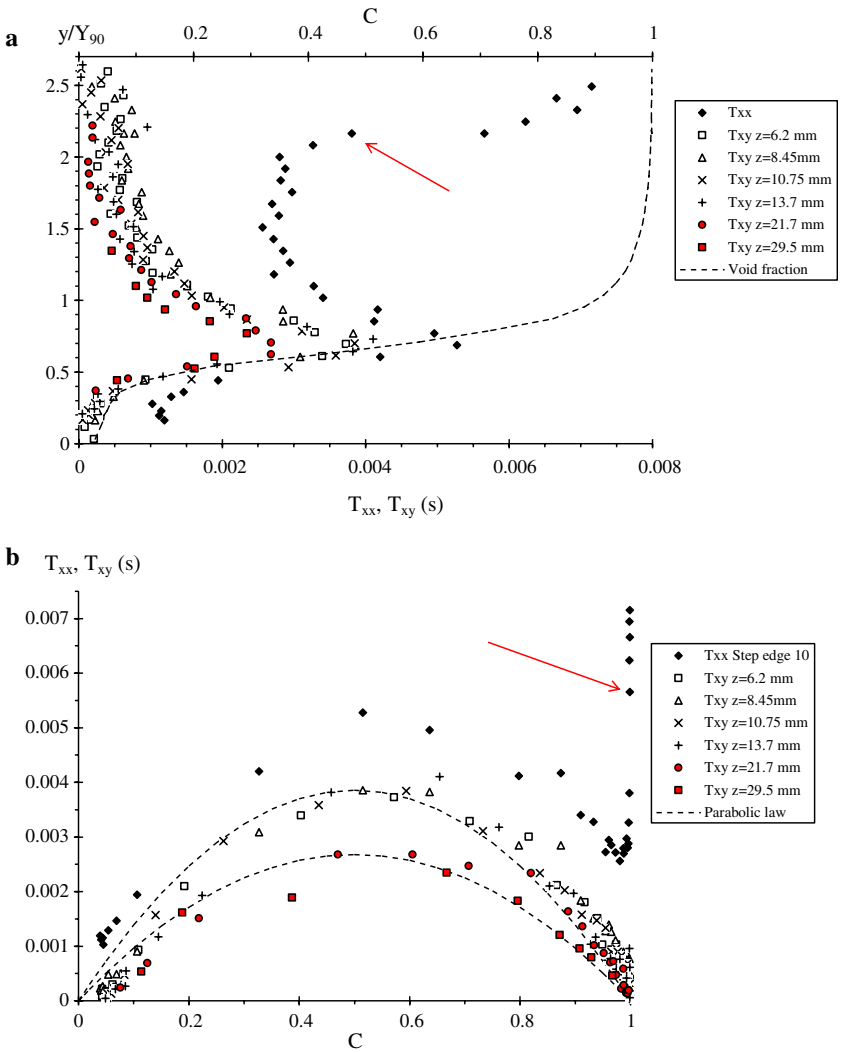

Fig. 7 Distributions of auto- and cross-correlation time scales T_{xx} and T_{xy} in skimming flows for several transverse separation distances Δz. **a** Normal distributions for d_c/h = 1.15, Re = 4.6E+5, single-tip probe (Ø = 0.35 mm), step edge 10. Comparison with the measured void fraction distribution. **b** Relationship between auto- and cross-correlation time scales and void fraction in a cross-section. Flow conditions: d_c/h = 1.15, Re = 4.6E+5, single-tip probe (Ø = 0.35 mm), step edge 10—comparison with Eq. 20

Figure 7b presents a typical relationship between void fraction and correlation time scales at a given flow cross-section. Both the distributions of auto- and cross-correlation time scales T_{xx} and T_{xy} presented a parabolic shape for $0 \leq C \leq 0.95$ at all step edges and for all investigated flow rates. This is seen in Fig. 7b. However a marked change of shape for the auto-correlation time scale T_{xx} distribution was systematically observed in the upper spray region ($C > 0.95$–0.97). This change in profile is highlighted in Fig. 7a, b with an arrow. It is suggested that the pattern may indicate a change of the spray structure in the upper spray region which consisted primarily of ejected droplets that did not interact with the rest of the flow.

The relationship between the cross-correlation time scale and the void fraction were closely fitted by:

$$\frac{T_{xy}}{(T_{xy})_{max}} = 4C(1-C) \quad (20)$$

where $(T_{xy})_{max}$ is the maximum cross-correlation time scale in the cross-section for a given separation distance Δz. Equation 20 is compared with experimental data in Fig. 7b. Experimental observations of maximum transverse time scale $(T_{xy})_{max}$ are reported in Table 2.

3.5 Turbulent time and length scales

The turbulent length and time scales, L_{xy} and $\mathbf{T}$, respectively, were calculated using Equs. 5 and 6 based upon correlation analyses conducted with several transverse separation distances Y. Typical results in terms of dimensionless turbulent length scale L_{xy}/Y_{90}, integral turbulent time scale $\mathbf{T}\sqrt{g/Y_{90}}$ and advection length scale L_{xx}/Y_{90} are presented in Fig. 8. The measured void fraction data are also shown in Fig. 8.

The turbulent length scale L_{xy} represents a characteristic dimension of the large vortical structures advecting the air bubbles and air–water packets. In bubbly flows, the turbulent length scales are closely linked with the characteristic sizes of the large-size eddies and their interactions with entrained air bubbles. This was evidenced by high-speed photographs demonstrating air bubble trapping in large eddies of developing mixing layers (e.g. Hoyt and Sellin 1989; Chanson 1997a). Herein the integral turbulent length scale L_{xy} represented a measure of the size of large vortical structures advecting air bubbles in the skimming flow regime. The air–water turbulent length scale was closely related to the characteristic air–water depth Y_{90}: i.e., $0.05 \leq L_{XV}/Y_{90} \leq 0.2$ (Fig. 8). This result was valid for both transverse and longitudinal length scales, and it was irrespective of the flow Reynolds numbers within the range of the experiments.

The turbulence time scale $\mathbf{T}$ characterises the integral turbulent time scale of the large eddies advecting the air bubbles and air–water particle clusters. The streamwise and transverse integral turbulent time scales were close, and the present data yielded typically $0.01 \leq \mathbf{T}\sqrt{g/Y_{90}} \leq 0.06$ (Fig. 8).

The advection length scale L_{xx} is a characteristic longitudinal size of the large advecting eddies. Within Taylor's hypothesis of separate and additive advection and diffusion processes, it would be expected that the

Table 2 Experimental observations of maxima of transverse cross-correlation time scale T_{xy} and of maximum cross-correlation $(R_{xy})_{max}$ in a cross-section as a function of the transverse separation distance

Q_w (m^3/s)	d_c/h	Re	Instrumentation	Step edge	Δz (mm)	Maximum $(R_{xy})_{max}$	$(T_{xy})_{max}$ (s)	Comments
0.116	1.15	4.6E+5	2 single-tip probes	10	0	1 (+)	0.0053 (+)	
					3.6	0.6339	0.005	Run 060508b
					6.3	0.4504	0.0037	Run 060412c
					8.45	0.4293	0.0039	Run 060411a
					10.75	0.3914	0.0038	Run 060411b
					13.7	0.3172	0.0041	Run 060411c
					16.7	0.3215	0.0039	Run 060412a
					21.7	0.2391	0.0027	Run 060412b
					29.5	0.182	0.0023	Run 060413a
					40.3	0.1516	0.0023	Run 060508a
0.161	1.45	6.4E+5	2 single-tip probes	10	0	1 (+)	0.0055 (+)	
					3.6	0.6493	0.0048	Run 060509a
					8.45	0.468	0.0041	Run 060511b
					13.7	0.37	0.0044	Run 060509b
					21.7	0.2845	0.0040	Run 060510a
					40.3	0.1417	0.0020	Run 060510b
					55.7	0.1166	0.0019	Run 060511a

d_c Critical flow depth, Re Reynolds number defined in terms of the hydraulic diameter, W channel width, (+) auto-correlation results

advection and turbulent length scales are about equal: $L_{xy} \approx L_{xx}$. The result was valid for $C < 0.95$, although some significant deviation was observed in the upper spray region ($C > 0.95$–0.97) (Fig. 8).

The relationships between the integral length scales L_{xy} and L_{xx} and integral time scale $\mathbf{T}$, and the void fraction exhibited a "skewed parabolic shape" with maxima occurring for void fractions between 0.6 and 0.7. This is illustrated in Fig. 9. The dimensionless distributions of transverse turbulent length scale L_{xy}/Y_{90}, transverse integral turbulent time scale $\mathbf{T}\sqrt{g/Y_{90}}$ and advection length scale L_{xx}/Y_{90} were best correlated by:

$$\frac{L_{xy}}{(L_{xy})_{max}} = 1.75C^{0.57}(1-C)^{0.324} \quad 0 \le C \le 1 \tag{21}$$

$$\frac{\mathbf{T}}{\mathbf{T}_{max}} = 1.97C^{0.59}(1-C)^{0.5} \quad 0 \le C < 0.97 \tag{22}$$

$$\frac{L_{xx}}{(L_{xx})_{max}} = 1.6C^{0.55}(1-C)^{0.3} \quad 0 \le C < 0.97 \tag{23}$$

where $(L_{xy})_{max}$, $\mathbf{T}_{max}$, and $(L_{xx})_{max}$ are the characteristic maxima in the cross-section. Experimental observations of $(L_{xy})_{max}$, $\mathbf{T}_{max}$, and $(L_{xx})_{max}$ are regrouped in Table 3. Equation (21) to (23) are compared with data in Fig. 9. Note that Equations (22) and (23) are not valid in the upper spray region ($C > 0.95$–0.97).

The high-velocity open channel flows on the stepped channel were highly turbulent (Fig. 4a). Present results demonstrated that the high levels of turbulence were associated directly with large scale turbulence. In particular, the intermediate region ($0.3 < C < 0.7$) between bubbly and spray regions seemed to play a major role in the development the large vortices. Turbulence level maxima were observed for $0.4 < C < 0.5$, while maximum integral turbulent scales were seen for $0.6 < C < 0.7$ (Fig. 9).

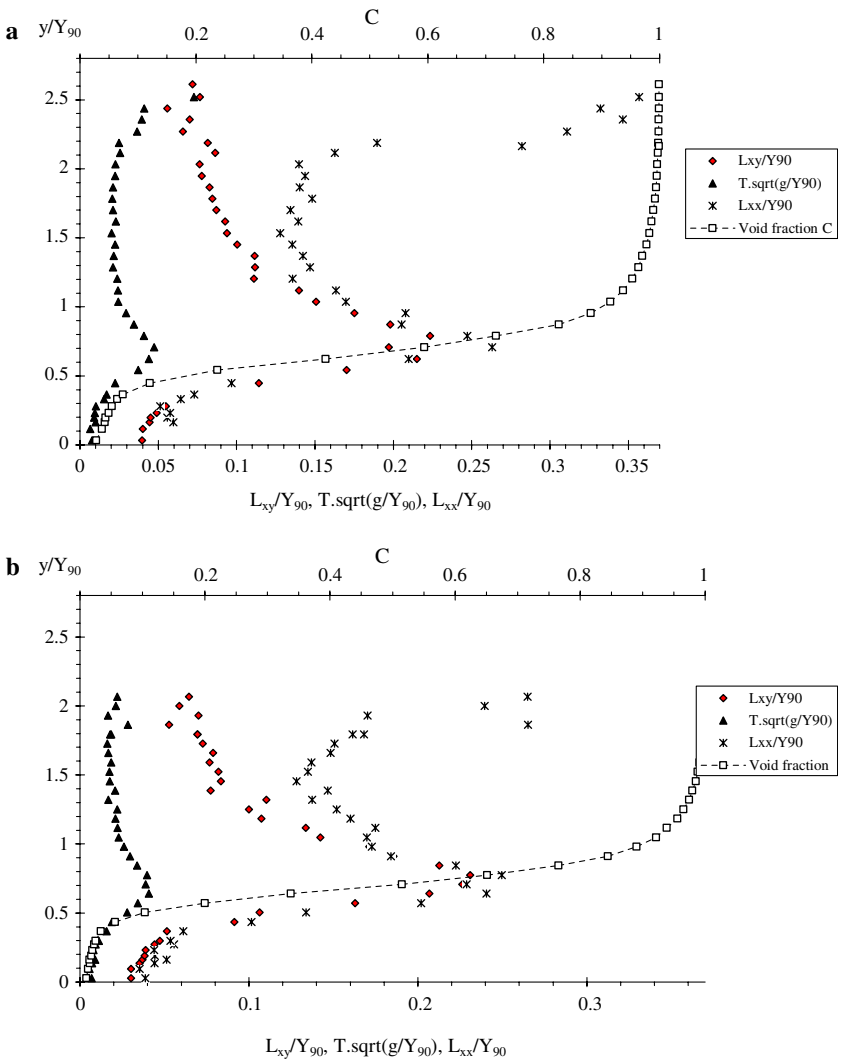

Fig. 8 Dimensionless distributions of air–water transverse turbulent length scales L_{xy}/Y_{90}, transverse integral turbulent time scale $\mathbf{T}_{max}\sqrt{g/Y_{90}}$ and advection length scale L_{xx}/Y_{90}. Single-tip probe (Ø = 0.35 mm). **a** $d_c/h = 1.15$, $Re = 4.6$ E+5, step edge 10. **b** $d_c/h = 1.45$, $Re = 6.4$E+5, step edge 10

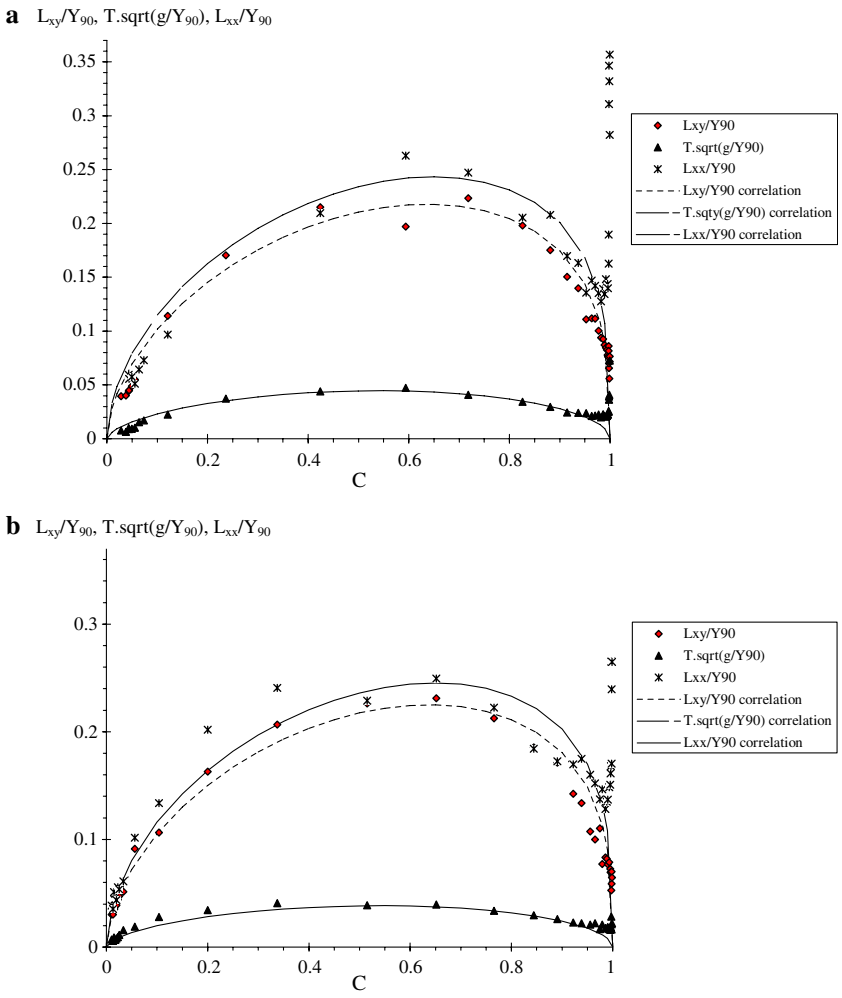

Fig. 9 Dimensionless relationship between transverse turbulent length scale L_{xy}/Y_{90}, transverse integral time scale $\mathbf{T}_{max}\sqrt{g/Y_{90}}$ and advection length scale L_{xx}/Y_{90}, and void fraction at Step 10. Single-tip probe (Ø = 0.35 mm)—comparison with Eq. 21–23. **a** d_c/h = 1.15, Re = 4.6E+5, step edge 10. **b** d_c/h = 1.45, Re = 6.4E+5, step edge 10

4 Discussion

4.1 The upper spray region

In the present study, detailed air–water flow measurements were conducted in the spray region (Fig. 10a) defined herein as $C > 0.7$ for void fractions C up to 0.999 corresponding to y/Y_{90} up to 2.5. The experimental data showed some distinctive features in the upper spray region defined as $C > 0.95$–0.97, especially in terms of droplet chord size distributions and advection integral length scale distributions.

In the lower spray region ($0.7 < C < 0.95$), the probability distribution functions of water chord were skewed with a preponderance of small droplets relative to the mean and they followed closely a log-normal distribution. The distributions of advection length scale L_{xx} showed a decrease in dimensionless length scales L_{xx}/Y_{90} with increasing distance y/Y_{90} and decreasing liquid fraction (1–C).

Some different results were observed in the upper spray region ($C > 0.95$–0.97). The probability distribution functions of droplet chords were relatively flat and did not follow a log-normal distribution. The PDF maxima were about 0.1–0.15 and most droplet chords were between 0.5 and 8 mm. For $C > 0.95$–0.97, the distributions of advection integral length scale showed increasing length scale with decreasing liquid fraction

Table 3 Characteristic integral turbulent length and time scales, and advection length scales in skimming flows on a stepped chute

Parameter	$d_c/h = 1.15$	$d_c/h = 1.45$	Remarks
Transverse scales ($Y = \Delta z$)			Single-tip probe (Ø = 0.35 mm)
$(L_{xy})_{max}/Y_{90}$	0.223	0.231	
$\mathbf{T}_{max}\sqrt{g/Y_{90}}$	0.0473	0.040	$0 \le C < 0.97$
$(L_{xx})_{max}/Y_{90}$	0.263	0.265	$0 \le C < 0.97$
Streamwise scales ($Y = \Delta x$)			Double-tip probe data (Ø = 0.25 mm)
$(L_{xy})_{max}/Y_{90}$	0.1865	0.151	
$\mathbf{T}_{max}\sqrt{g/Y_{90}}$	0.0472	0.041	$0 \le C < 0.97$
$(L_{xx})_{max}/Y_{90}$	0.231	0.132	$0 \le C < 0.97$

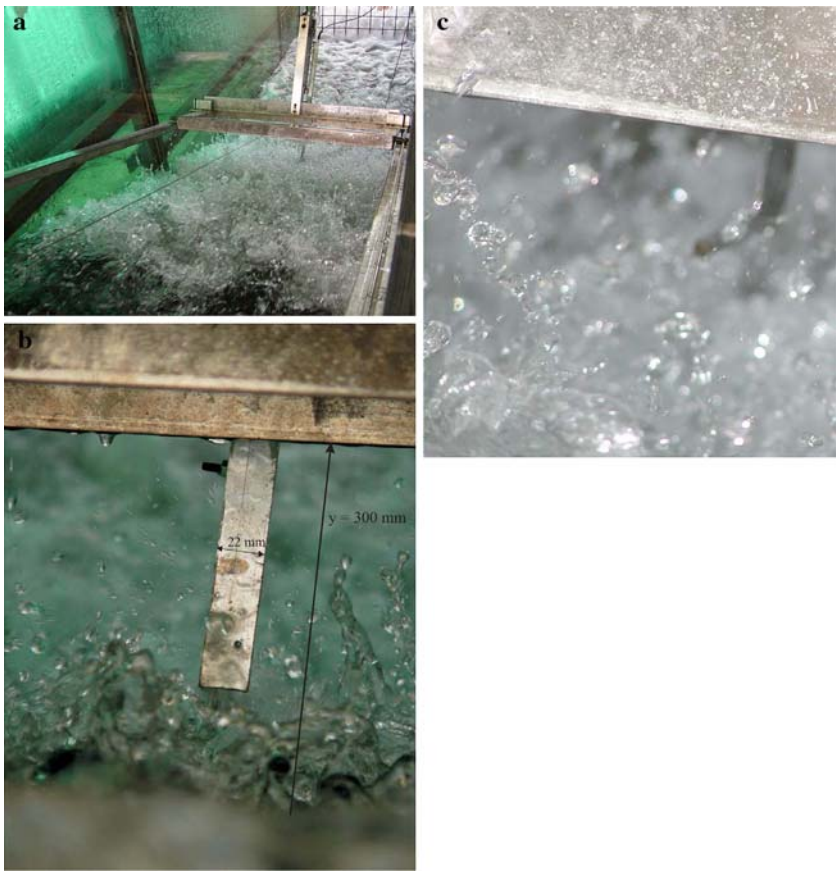

Fig. 10 High-speed photographs of ejected water droplets in ballistic trajectory in the upper spray region viewed from upstream. **a** d_c/h = 1.33, *Re* = 5.7E+5 (shutter speed: 1/400 s)—looking downstream from above at the spray region. **b** d_c/h = 1.33, *Re* = 5.7E+5 (shutter speed: 1/320 s)—the distance *y* between the pseudo-bottom formed by the step edges and the lower trolley support is shown. **c** d_c/h = 1.35, *Re* = 6.2E+5 (shutter speed 1/200 s)—details of ejected droplets—note the double-tip probe in background

(1–*C*) (Figs. 8, 9). The result might suggest the existence of longitudinal ''streaks'' of water drops.

It is believed that the contrasting features of the upper spray region reflected a change in the microscopic flow structure. That is, the upper spray region consisted primarily of ejected water droplets that did not interact with the main flow nor with the surrounding air. These droplets tended to follow some ballistic trajectory as illustrated in Fig. 10b, c. Their ''history'' was dominated by the initial ejection process and possibly by droplet collisions.

4.2 Self-similarity in air–water flow properties

A self-similar process is one whose spatial distribution of properties at various times can be obtained from one another by a similarity transformation (Barenblatt 1994, 1996). Self-similarity is a powerful tool in turbulence flow research, and skimming flows on a stepped chute are one type of turbulent flows involving a wide spectrum of spatial and temporal scales. The nonlinear interactions among vortices and particles at different scales lead to a complicated flow structure, and relationships among flows at different scales are of crucial significance. These play also a major role in comparing analytical, experimental and numerical results as these results are for different scales. For example, most stepped spillway applications are for prototype flow conditions with flow Reynolds number between 1E+6 and more than 1E+9 that cannot be modelled numerically nor physically.

In the present study, self-similarity was observed in terms of the distributions of air–water flow properties. Table 4 summarises some basic self-similarity equations that were observed during the present work. Self-similarity is illustrated for example in Figs. 3, 4b, 5, 7a, 9, and 11. These self-similar relationships were observed at both macroscopic and microscopic levels. For example, the distributions of void fraction and interfacial velocity at a macroscopic level, and the cross-correlation function and probability distribution functions of particle chords at a microscopic level (Table 4).

Self-similarity is closely linked with dynamic similarity. Some researchers argued that it is nearly impossible to achieve a true dynamic similarity in stepped spillway models because of number of relevant dimensionless parameters (Boes 2000; Chanson 2001; Chanson and Gonzalez 2005). However the present experimental results showed a number of self-similar

relationships that remain invariant under changes of scale: i.e., they have scaling symmetry which led in turn to remarkable application at prototype scales (Table 4). Clearly the present results are most significant. They provide a picture general enough to be used, as a first approximation, to characterise the air–water flow field in similar stepped spillway structures irrespective of the physical scale.

5 Conclusion

Detailed gas–liquid flow measurements were performed in high-velocity open channel flows above a steep stepped channel. The experiments were conducted with flow Reynolds numbers ranging from 3.8E+5 to 7.1E+5, and measurements were performed with phase-detection intrusive probes: single-tip conductivity probes (Ø = 0.35 mm) and double-tip conductivity probes (Ø = 0.25 mm). An advanced signal processing technique with new signal correlation analyses was developed and applied systematically.

The air water flow properties presented some basic characteristics that were qualitatively and quantitatively similar to previous studies in skimming flows. These included the distributions of void fraction, bubble count rate and interfacial velocity. Some self-similar relationships were observed systematically at both macroscopic and microscopic levels (Table 4). These included the distributions of void fraction, bubble count rate, interfacial velocity and turbulence level at a macroscopic scale, and the bubble chord distributions and auto- and cross-correlation functions at the microscopic level. The experimental results showed a number of self-similar relationships that remained invariant under changes of scale. The present findings are significant because they provides a picture general enough to characterise the air–water flow field in prototype stepped spillways.

The correlation analyses yielded a characterisation of the large eddies advecting the bubbles. Basic results included the integral turbulent length and time scales. The turbulent length scales characterised some measure of the size of large vortical structures advecting air bubbles in the skimming flows, and the data were closely related to the characteristic air–water depth Y_{90}: i.e. $L_{xy}/Y_{90} \approx 0.05$–$0.2$. The dimensionless integral turbulent time scales were within $0.01 \leq \mathbf{T}\sqrt{g/Y_{90}} \leq 0.06$. The results were irrespective of the Reynolds numbers within the range of the experiments. The measurements highlighted further some maximum turbulence intensities, and maximum integral time and length scales in the intermediate region between the spray and bubbly flow regions (i.e. $0.3 < C < 0.7$). The findings suggested that turbulent dissipation by large-scale vortices may be a significant process in the intermediate zone.

In the spray region, present results highlighted the existence of an upper spray region for $C > 0.95$–0.97 in which the distributions of droplet chord sizes and

Table 4 Self-similarity of the air–water flow properties in skimming flow above stepped chutes

Flow property	Self-similarity	Remarks
Void fraction distribution	$C = 1 - \tanh^2(\chi)$	$\chi = K' - \frac{y'}{2D_o} + \frac{\left(y'-\frac{1}{3}\right)^3}{3D_o} 0 \leq y' \leq 1$, Eq. 10.
Bubble count rate distribution	$\frac{F}{F_{max}} = 4C(1-C)$	$0 \leq C \leq 1$, Eq. 14
Interfacial velocity distribution	$\frac{V}{V_{90}} = y'^{1/N}$	$0 \leq y' \leq 1$, Eq. 15.
	$\frac{V}{V_{90}} = 1$	$1 \leq y' \leq 2.5$, Eq. 16
Turbulence level distribution	$\mathrm{Tu} = 0.25 + a\left(\frac{Fd_c}{V_c}\right)^b$	$0 \leq C \leq 1$, Eq. 17
Probability distribution functions of bubble chords	Log-normal distribution	$0 \leq C \leq 0.3$
Probability distribution functions of droplet chords	Log-normal distribution	$0.7 \leq C \leq 0.95$
Cross-correlation function	$R_{xx} = \frac{1}{1+\left(\frac{\tau}{T_{0.5}}\right)^{1.3}}$	$0 \leq y' \leq 1$, Eq. 18
Cross-correlation function (between two probe sensors separated by a distance Y)	$\frac{R_{xy}}{(R_{xy})_{max}} = exp\left(-\frac{1}{1443}\frac{(\tau-T)^2}{\tau_{0.5}}\right)$	$0 \leq y' \leq 1$, Eq. 19. Both transverse and streamwise probe sensor separations
Cross-correlation time scale distribution (between two probe sensors separated by a distance Y)	$\frac{T_{xy}}{(T_{xy})_{max}} = 4C(1-C)$	$0 \leq C \leq 1$, Eq. 20. Both transverse and streamwise probe sensor separations
Distribution of transverse integral turbulent length scale	$\frac{L_{xy}}{(L_{xy})_{max}} = 1.75C^{0.57}(1-C)^{0.324}$	$0 \leq C \leq 1$, Eq. 21.
Distribution of transverse integral turbulent time scale	$\frac{\mathbf{T}}{\mathbf{T}_{max}} = 1.97C^{0.59}(1-C)^{0.5}$	$0 \leq C \leq 0.97$, Eq. 22
Distribution of advection turbulent length scale	$\frac{L_{xx}}{(L_{xx})_{max}} = 1.6C^{0.55}(1-C)^{0.3}$	$0 \leq C \leq 0.97$, Eq. 23

$y' = y/Y_{90}$

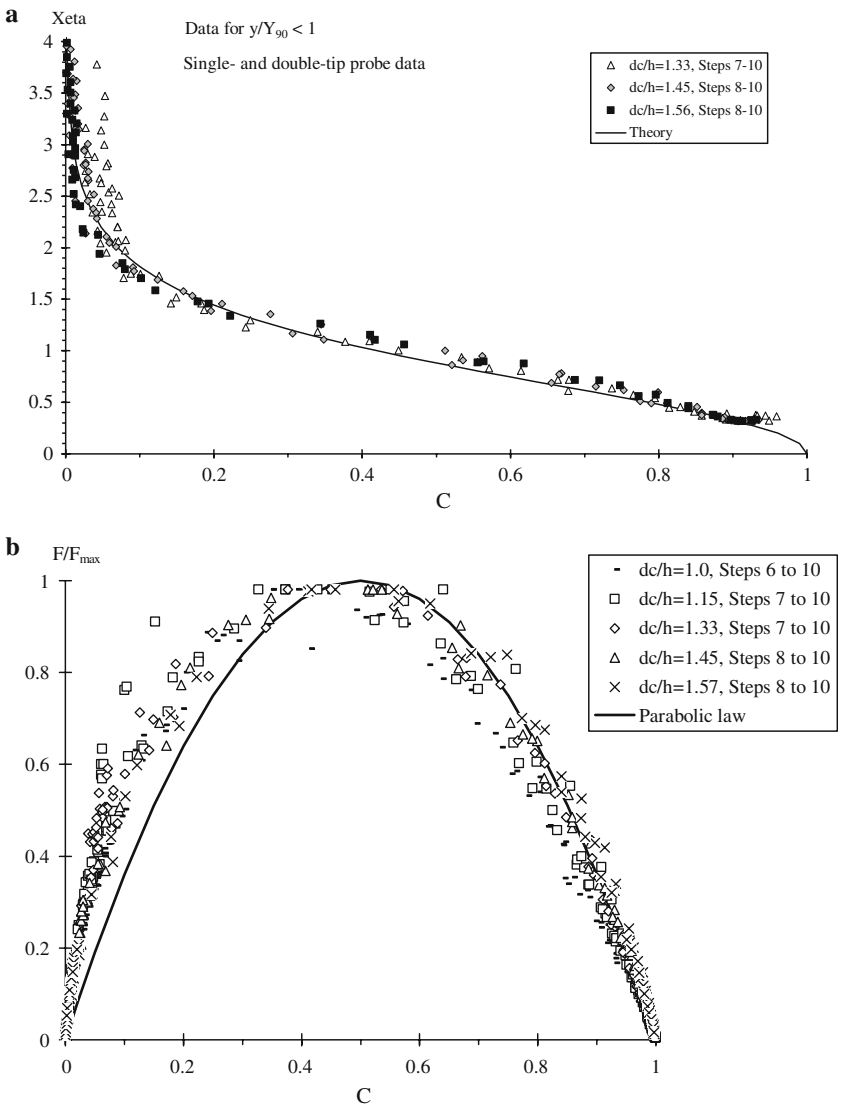

Fig. 11 Self-similarity in air–water skimming flows on a stepped chute. **a** Dimensionless void fraction distributions: $C = 1 - \tanh^2(\chi)$ with $\chi = K' - y'/(2D_o) + (y' - 1/3)^3/3D_o$). **b** Dimensionless bubble count rate distributions: $F/F_{max} = 4C(1 - C)$

integral advection scales (T_{xx}, L_{xx}) presented some marked differences. It is suggested that these patterns highlighted a change in spray structure, whereby the upper spray region consisted primarily of ejected droplets following ballistic trajectories.

Acknowledgments The writers acknowledges the technical assistance of Graham ILLIDGE and Clive BOOTH.

References

Amador A, Sanchez-Juny M, Dolz J, Sanchez-Tembleque F, Puertas J (2004) Velocity and pressure measurements in skimming flow in stepped spillways. In: Proceedings of the international conference on hydraulics of dams and river structures, Tehran, Iran, Balkema Publ., Netherlands, pp 279–285

Barenblatt GI (1994) Scaling, phenomena in fluid mechanics. Inaugural lecture delivered before the University of Cambridge on 3 May 1993, Cambridge University Press, UK, 49 pp

Barenblatt GI (1996) Scaling, self-similarity, and intermediate asymptotics. Cambridge University Press, UK, 386 pp

Boes RM (2000) Scale effects in modelling two-phase stepped spillway flow. In: Proceedings of the international workshop on hydraulics of stepped spillways, Balkema Publ., Zürich, Switzerland, pp 53–60

Cain P, Wood IR (1981a) Instrumentation for aerated flow on spillways. J Hydraul Div 107:1407–1424

Cain P, Wood IR (1981b) Measurements of self-aerated flow on a spillway. J Hydraul Div 107:1425–1444

Carosi G, Chanson H (2006) Air–water time and length scales in skimming flows on a stepped spillway. Application to the spray characterisation. Report no. CH59/06, Division of Civil Engineering, The University of Queensland, Brisbane, Australia, July, 142 pp

Chang KA, Lim HJ, Su CB (2003) Fiber optic reflectometer for velocity and fraction ratio measurements in multiphase flows. Rev Scientific Instrum 74:3559–3565, Discussion: 2004, 75:284–286

Chanson H (1997b) Air bubble entrainment in open channels. Flow structure and bubble size distributions. Int J Multiphase Flow 23:193–203

Chanson H (1997a) Air bubble entrainment in free-surface turbulent shear flows. Academic, London, UK, 401 pp

Chanson H (2001) The hydraulics of stepped chutes and spillways. Balkema, Lisse, The Netherlands, 418 pp

Chanson H (2002) Air–water flow measurements with intrusive phase-detection probes. Can we Improve their interpretation? J Hydraul Eng 128:252–255

Chanson H, Gonzalez CA (2005) Physical modelling and scale effects of air–water flows on stepped spillways. J Zhejiang Univ Sci 6A:243–250

Chanson H, Toombes L (1997) Flow aeration at stepped cascades. Research report no. CE155, Department of Civil Engineering, University of Queensland, Australia, June, 110 pp

Chanson H, Toombes L (2002) Air–water flows down stepped chutes: turbulence and flow structure observations. Int J Multiphase Flow 27:1737–1761

Crowe C, Sommerfield M, Tsuji Y (1998) Multiphase flows with droplets and particles. CRC Press, Boca Raton, USA, 471 pp

Euh DJ, Yun BJ, Song CH (2006) Benchmarking of the five-sensor probe method for a measurement of an interfacial area concentration. Exp Fluids 41:463–478

Gonzalez CA (2005) An experimental study of free-surface aeration on embankment stepped chutes. Ph.D. thesis, Department of Civil Engineering, The University of Queensland, Brisbane, Australia, 240 pp

Hayes MH (1996) Statistical, digital signal processing and modeling. Wiley, New York, USA

Herringe RA, Davis MR (1974) Detection of instantaneous phase changes in gas–liquid mixtures. J Phys E: Sci Inst 7:807–812

Hoyt JW, Sellin RHJ (1989) Hydraulic jump as 'mixing layer'. J Hydraul Eng 115:1607–1614

Jones OC, Delhaye JM (1976) Transient and statistical measurement techniques for two-phase flows: a critical review. Int J Multiphase Flow 3:89–116

Kim S, Fu XY, Wang X, Ishii M (2000) Development of the miniaturized four-sensor conductivity probe and the signal processing scheme. Int J Heat Mass Transf 43:4101–4118

Ohtsu I, Yasuda Y (1997) Characteristics of flow conditions on stepped channels. In: Proceedings of the 27th IAHR Biennial Congress, San Francisco, USA, Theme D, pp 583–588

Ruff JF, Frizell KH (1994) Air concentration measurements in highly-turbulent flow on a steeply-sloping chute. In: Proceedings of the hydraulic engineering conference, vol 2. ASCE, Buffalo, USA, pp 999–1003

Toombes L (2002) Experimental study of air–water flow properties on low-gradient stepped cascades. Ph.D. thesis, Department of Civil Engineering, The University of Queensland, Brisbane, Australia